Supplemental Material: Twist angle-dependent valley polarization of intralayer moiré excitons in van der Waals superlattices

Renqi Wang,[1] Kai Chang,[2,3] Wenhui Duan,[1,4,5] Yong Xu,[1,5,6,*] and Peizhe Tang[7,8,†]

[1] *State Key Laboratory of Low-Dimensional Quantum Physics and Department of Physics, Tsinghua University, Beijing,100084, China*
[2] *Center for Quantum Matter, Zhejiang University, Hangzhou 310058, China*
[3] *School of Physics, Zhejiang University, Hangzhou 310058, China*
[4] *Institute for Advanced Study, Tsinghua University, Beijing 100084, China*
[5] *Frontier Science Center for Quantum Information, Beijing, 100084, China*
[6] *RIKEN Center for Emergent Matter Science (CEMS), Wako, Saitama, 351-0198, Japan*
[7] *School of Materials Science and Engineering, Beihang University, Beijing 100191, China*
[8] *Max Planck Institute for the Structure and Dynamics of Matter, Center for Free Electron Laser Science, 22761 Hamburg, Germany*

CONTENTS

* yongxu@mail.tsinghua.edu.cn
† peizhet@buaa.edu.cn

S1. DETAILS OF THE CONTINUUM MODEL AND THE PARAMETERS FROM DFT STUDIES

The continuum model of the moiré system used in this article can be formulated as a $\mathbf{k}\cdot\mathbf{p}$ model of monolayer transition metal dichalcogenides (TMD) [1] in the moire potential provided by the interlayer coupling [2]

$$\hat{H}(\mathbf{k}) = \hbar v_F(\tau q_x\hat{\sigma}_x + q_y\sigma_y) + \frac{E_g}{2}\sigma_z + \Delta(\mathbf{r}) \tag{S1}$$

where $\hbar$ is the reduced Planck constant, the velocity parameter v_F is related to nearest neighbor coupling between transition metal orbitals, τ is the valley index, $\mathbf{q} = \mathbf{k} - \tau\mathrm{K}$ is the vector from the valley τK to any momentum $\mathbf{k}$ in the Brillouin zone (BZ), and the E_g stands for the direct band gap in the monolayer TMD. We use $\hbar v_F = 3.9$ eV·Å [1] and $E_g = 2.05$ eV [3] in this article. The $\Delta(\mathbf{r})$ is the moiré potential. For small twist angles θ, the different position $\mathbf{r}$ in the heterobilayer moiré lattice can be characterized by the in-plane displacement $\mathbf{d} = \theta\hat{z}\times\mathbf{r}$ [4, 5]. Therefore,

$$\Delta(\mathbf{r}) \approx \Delta[\mathbf{d}(\mathbf{r})] \approx \sum_j V_j \exp(i\mathbf{G}_j\cdot\mathbf{d}) = \sum_j V_j \exp(i\mathbf{b}_j\cdot\mathbf{r}) \tag{S2}$$

where $\mathbf{G}_j$ is the reciprocal lattice vector of a monolayer TMD and $\mathbf{b}_j = \theta\mathbf{G}_j\times\hat{z}$ represents the moiré reciprocal lattice vector. Constrained by the three-fold rotational symmetry around the $\hat{z}$-axis and the requirement that $\Delta(\mathbf{r})$ be a real number, we have $V_1 = V_3 = V_5 = V_2^* = V_4^* = V_6^*$. In this study, we use a diagonalized moiré potential $V_1 = \mathrm{diag}(V_c e^{i\phi_c}, V_v e^{i\phi_v})$ [2], where the superscripts c and v indicate the electrostatic potential acting on d-orbitals corresponding to the conduction and valence bands, respectively.

In the momentum space, this Hamiltonian can be written in a more specific form which can be easily diagonalized to obtain the eigenenergies and eigenvectors

$$H_{\mathbf{b},\mathbf{b}'}(\mathbf{k}) = [\hbar v_F(\tau(q_x+b_x)\hat{\sigma}_x + (q_y+b_y)\sigma_y) + \frac{E_g}{2}\sigma_z]\delta_{\mathbf{b},\mathbf{b}'} + \sum_i V_i\delta_{\mathbf{b}-\mathbf{b}',\mathbf{b}_i} \tag{S3}$$

To calculate the moiré electronic structures for the WSe_2 layer, we need to solve the effective continuum models around the K and -K valleys ($\tau = 1$ and -1) of the untwisted TMD, and then fold them into the moiré BZ [see Fig. S3(a), where the blue region represents the continuum model with $\tau = 1$ and red region represents continuum model with $\tau = -1$. The two regions are far separated in momentum space, so the two continuum models are decoupled at the single-particle level]. We will denote valleys in BZ as $\pm$K while valleys in the moiré BZ as κ and κ'. For simplicity, We also use $\pm$K to denote continuum models with $\tau = \pm 1$ somewhere.

To obtain the moiré potential parameters (V^i, ϕ^i), $(i = v, c)$, we make use of the density functional theory (DFT) software VASP [6–8] with the spin-orbit coupling (SOC) to calculate the WSe_2/WS_2 heterobilayer systems. The moiré potential acting on d-orbitals of corresponding valence and conduction bands can be interpreted as the variation of the valence band maximum (VBM) and the conduction band minimum (CBM) as a function of position $\mathbf{r}$ in the moiré superlattice. As discussed above, these variations can be mapped to the changes in the VBM and CBM with different interlayer displacements $\mathbf{d}$ in AA stacked WSe_2/WS_2 bilayer with zero twist angle.

Herein, we calculate the band structure of three high-symmetry stacking configurations [5]. The three configurations are denoted as Se/W, AA, and W/S, based on the alignment of the metal atom and chalcogen atom in the opposite layers. For instance, Se/W indicates that the Se atom in the top layer is aligned with the W atom in the bottom layer. The vacuum distance is set to be 20 Å in the slab model and the interlayer distances in different structure configurations are obtained by

structural relaxation. In each calculation, we employ the Perdew-Burke-Ernzerhof (PBE) functional [9] and set the **k**-point sampling to be $12 \times 12 \times 1$ in the BZ to achieve energy convergence up to 1 meV/atom. Through orbital projection calculations, we identify the electronic bands with orbital characters corresponding to the WSe_2 A exciton. The band minima or maxima of these bands relative to the vacuum can be used to fit the moiré potential [10]. The moiré potential parameters fitted from the three configurations are $(V^c, \phi^c) = (12\,\text{meV}, -136^\circ)$ and $(V^v, \phi^v) = (15\,\text{meV}, -45^\circ)$.

S2. BETHE-SALPETE EQUATIONS

The eigenvalues and eigenvectors of the moiré continuum Hamiltonian at momentum $\mathbf{k}$, $H_{\mathbf{b},\mathbf{b}'}(\mathbf{k})$, in the n-th band are denoted as $E_{n\mathbf{k}}$ and $U_{\mathbf{b},n}(\mathbf{k})$, respectively. The eigenvectors $U_{\mathbf{b},n}(\mathbf{k})$ lead to the Bloch eigenstates

$$\psi_{n\mathbf{k}}(\mathbf{r}) = \sum_{\mathbf{b}} e^{i(\mathbf{k}+\mathbf{b})\cdot\mathbf{r}} U_{\mathbf{b},n}(\mathbf{k}) \tag{S4}$$

Based on these Bloch orbitals, the Hamiltonian matrix elements of Bethe-Salpete equations (BSE) [11–14] with the center-of-mass exciton momentum $\mathbf{Q}$ can be further constructed

$$H^{exc}_{vc\mathbf{k},v'c'\mathbf{k}'}(\mathbf{Q}) = (E_{c\mathbf{k}+\mathbf{Q}} - E_{v\mathbf{k}})\delta_{c,c'}\delta_{v,v'}\delta_{\mathbf{k},\mathbf{k}'} + \left[\bar{V}_{v\mathbf{k}c\mathbf{k}+\mathbf{Q},v'\mathbf{k}'c'\mathbf{k}'+\mathbf{Q}} - W_{v\mathbf{k}c\mathbf{k}+\mathbf{Q},v'\mathbf{k}'c'\mathbf{k}'+\mathbf{Q}}\right] \tag{S5}$$

where c and v correspond to conduction and valence bands and the specific form of the BSE kernel matrix elements can be written as

$$\begin{aligned}
W_{v\mathbf{k}c\mathbf{k}+\mathbf{Q},v'\mathbf{k}'c'\mathbf{k}'+\mathbf{Q}} &= \frac{1}{\Omega}\sum_{\mathbf{g},\mathbf{g}'}\langle c\mathbf{k}+\mathbf{Q}|e^{i(\mathbf{q}+\mathbf{g})\cdot\mathbf{r}}|c'\mathbf{k}'+\mathbf{Q}\rangle W_{\mathbf{g},\mathbf{g}'}(\mathbf{q},\omega)\langle v'\mathbf{k}'|e^{-i(\mathbf{q}+\mathbf{g}')\cdot\mathbf{r}}|v\mathbf{k}\rangle\delta_{\mathbf{q},\mathbf{k}-\mathbf{k}'} \\
&= \frac{1}{\Omega}\sum_{\mathbf{g},\mathbf{b},\mathbf{b}'} U^*_{\mathbf{b}+\mathbf{g},c}(\mathbf{k}+\mathbf{Q})U_{\mathbf{b},c'}(\mathbf{k}'+Q)W_{RK}(|\mathbf{q}+\mathbf{g}|)U^*_{\mathbf{b}',v'}(\mathbf{k}')U_{\mathbf{b}'+\mathbf{g},v}(\mathbf{k})\delta_{\mathbf{q},\mathbf{k}-\mathbf{k}'} \\
\bar{V}_{v\mathbf{k}c\mathbf{k}+\mathbf{Q},v'\mathbf{k}'c'\mathbf{k}'+\mathbf{Q}} &= \frac{1}{\Omega}\sum_{\mathbf{g}\neq 0}\langle c\mathbf{k}+\mathbf{Q}|e^{i(\mathbf{Q}+\mathbf{g})\cdot\mathbf{r}}|v\mathbf{k}\rangle v(\mathbf{Q}+\mathbf{g})\langle v'\mathbf{k}'|e^{-i(\mathbf{Q}+\mathbf{g})\cdot\mathbf{r}}|c'\mathbf{k}'+\mathbf{Q}\rangle \\
&= \frac{1}{\Omega}\sum_{\mathbf{g}\neq 0,\mathbf{b},\mathbf{b}'} U^*_{\mathbf{b}+\mathbf{g},c}(\mathbf{k}+\mathbf{Q})U_{\mathbf{b},v}(\mathbf{k})v(\mathbf{Q}+\mathbf{g})U^*_{\mathbf{b}',v'}(\mathbf{k}')U_{\mathbf{b}'+\mathbf{g},c'}(\mathbf{k}'+\mathbf{Q})
\end{aligned} \tag{S6}$$

Herein, $|n\mathbf{k}\rangle$ is the Bloch state, Ω is the normalized area, and $\mathbf{g}$ is the moiré reciprocal lattice vector to be summed over. The term $W_{vc\mathbf{k},v'c'\mathbf{k}'}$ is called the direct attraction term [see Fig. 3(a) in the main text], describing a scattering process between an electron and a hole where a virtual photon scatters the electron to an electron and the hole to a hole, satisfying the conservation of momentum. $W_{RK}(\mathbf{q}) = \frac{e^2}{\varepsilon}\frac{2\pi}{q(1+qr_0)}$ is Rytova-Keldysh potential, which is widely used in 2D materials considering the Coulomb screening [15–17]. In this work, we set the average permittivity of the environment $\varepsilon = 1.5$ and the screening length $r_0 = 38.0\,\text{Å}$ [18] in the main text. $U_{\mathbf{b},n}(\mathbf{k})$ is the Bloch eigenvector solved from the continuum model. On the other hand, the term $\bar{V}_{vc\mathbf{k},v'c'\mathbf{k}'}$ is called the exchange term which contributes to the processes of the annihilation and creation of electron-hole pairs at different momenta through a virtual photon, and $v(\mathbf{q}) = \frac{2\pi e^2}{q}$ is the bare 2D Coulomb potential.

The exciton eigenenergy $\Omega^S_{\mathbf{Q}}$ and exciton wavefunctions in momentum space $A^{S\mathbf{Q}}_{cv\mathbf{k}}$ satisfy the Bethe-Salpete equations

$$\sum_{v'c'\mathbf{k}'} H^{exc}_{vc\mathbf{k},v'c'\mathbf{k}'}(\mathbf{Q})A^{S\mathbf{Q}}_{c'v'\mathbf{k}'} = \Omega^S_{\mathbf{Q}}A^{S\mathbf{Q}}_{cv\mathbf{k}} \tag{S7}$$

where S represents the index of the excitons. The real space exciton wavefunctions can be described in the basis of electron-hole pairs through $A^{S\mathbf{Q}}_{cv\mathbf{k}}$

$$\Psi_{S\mathbf{Q}}(\mathbf{r}_e,\mathbf{r}_h)=\sum_{cv\mathbf{k}} A^{S\mathbf{Q}}_{vc\mathbf{k}}\psi_{c\mathbf{k}+\mathbf{Q}}(\mathbf{r}_e)\psi^*_{v\mathbf{k}}(\mathbf{r}_h) \tag{S8}$$

and the absorption spectra can be expressed as [11]

$$Im[\epsilon_M(\omega)]=Im\left[1-\frac{1}{\Omega}\lim_{\mathbf{q}\to 0}v(\mathbf{q})\sum_S \frac{|\sum_{cv\mathbf{k}} A^S_{cv\mathbf{k}}\langle v\mathbf{k}-\mathbf{q}|e^{-i\mathbf{q}\cdot\mathbf{r}}|c\mathbf{k}\rangle|^2}{\omega-\Omega_S+i\eta}\right] \tag{S9}$$

S3. SPIN-SINGLET AND SPIN-TRIPLET MOIRÉ EXCITONS

When we consider the continuum models near both K and -K valleys, four types of electron-hole pairs can be identified according to the valley origin of the electron and hole. For example, The pair where electron and hole are both from the K valley can be denoted as $|c,\mathrm{K};v,\mathrm{K}\rangle$. Similarly we can define the $|c,-\mathrm{K};v,-\mathrm{K}\rangle, |c,\mathrm{K};v,-\mathrm{K}\rangle, |c,-\mathrm{K};v,\mathrm{K}\rangle$. The electron and hole in the last two types of electron-hole pairs are from opposite valleys. Due to the spin-valley locking in the original untwisted TMD materials [see Fig. S3(a)], $|c,\mathrm{K};v,\mathrm{K}\rangle$ and $|c,-\mathrm{K};v,-\mathrm{K}\rangle$ can contribute to the spin-singlet bright moiré excitons, while $|c,\mathrm{K};v,-\mathrm{K}\rangle$ and $|c,-\mathrm{K};v,\mathrm{K}\rangle$ can contrinute to the spin-triplet dark moiré excitons.

We can analyze the coupling between these four electron-hole pairs through direct or exchange Coulomb interactions. For the $|c,\mathrm{K};v,\mathrm{K}\rangle$ and $|c,-\mathrm{K};v,-\mathrm{K}\rangle$, the direct Coulomb attraction between an electron and a hole does not couple them [see Fig. 3(b) in the main text]. This is because the scattering amplitude for an electron to be scattered to the opposite valley, which requires virtual photons with large wave vectors, is much smaller than that within the same valley. We can neglect this process in the following calculations. Conversely, the exchange interactions describe the scattering process of annihilation and creation of electron-hole pairs at different $\mathbf{k}$ points, without requiring a virtual photon with a large wave vector. Therefore, the annihilation of an electron-hole pair in the K valley and the creation of a pair in the -K valley are of the same order as processes within the same valley. This interaction enables the coupling for states at different valleys. For the $|c,\mathrm{K};v,-\mathrm{K}\rangle$ or $|c,-\mathrm{K};v,\mathrm{K}\rangle$, neither direct nor exchange interactions can couple them to other types of electron-hole pairs, and the corresponding matrix elements $W_{vc\mathbf{k},v'c'\mathbf{k}'}$ and $\bar{V}_{vc\mathbf{k},v'c'\mathbf{k}'}$ are both zero. The specific coupling details can be found in the table below.

	$\lvert c,\mathrm{K};v,\mathrm{K}\rangle$	$\lvert c,-\mathrm{K};v,-\mathrm{K}\rangle$	$\lvert c,-\mathrm{K};v,\mathrm{K}\rangle$	$\lvert c,\mathrm{K};v,-\mathrm{K}\rangle$
$\lvert c,\mathrm{K};v,\mathrm{K}\rangle$	Direct & Exchange	Exchange	×	×
$\lvert c,-\mathrm{K};v,-\mathrm{K}\rangle$	Exchange	Direct & Exchange	×	×
$\lvert c,-\mathrm{K};v,\mathrm{K}\rangle$	×	×	Direct	×
$\lvert c,\mathrm{K};v,-\mathrm{K}\rangle$	×	×	×	Direct

TABLE S1. The coupling details between the four types of electron-hole pairs defined through their valley origin. The table shows which kind of interaction can contribute to the coupling. The label of × means neither direct or exchange interaction can lead to the coupling.

Therefore, the BSE Hamiltonian can be block diagonalized according to the coupling rules for different electron-hole pairs shown above. In the main text, we mainly discuss the block $|c,\mathrm{K};v,\mathrm{K}\rangle$ and $|c,-\mathrm{K};v,-\mathrm{K}\rangle$, corresponding to the bright spin-singlet excitons, which are the focus of optical experiments. However, we would like to note that the electron-hole pairs of $|c,\mathrm{K};v,-\mathrm{K}\rangle$ and

$|c, -\mathrm{K}; v, \mathrm{K}\rangle$ are also of great importance to understand the complete landscape of the moiré excitons, despite being optically inactive, since the ordering of bright and dark excitons and the exciton dispersion can influence the exciton dynamics and the temperature-dependent optical behavior [19] and we will discuss below.

S4. CONVERGENCE OF THE CALCULATIONS

The convergence of the number of conduction and valence bands considered for constructing the BSE Hamiltonian in our article is tested on the spin-singlet moiré excitons from two perspectives. At different twist angles, the number of conduction/valence bands used in the calculations of spin-triplet moiré excitons is the same as spin-singlet ones.

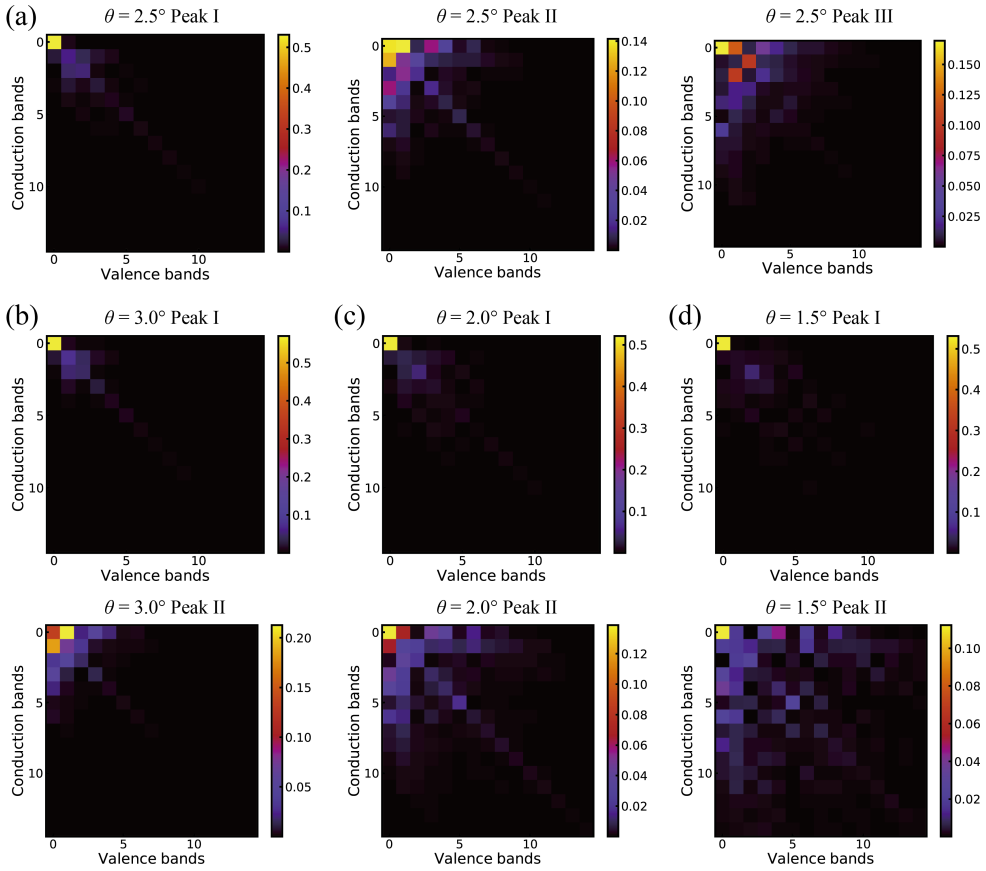

FIG. S1. The exciton amplitudes projected onto the conduction and valence bands in the continuum model near the K valley. (a) Exciton amplitudes of the three bright intralayer moiré excitons at $\theta = 2.5°$. The three peaks are shown in FIG. 2 (e) in the main text. (b-d) Exciton amplitudes of the first two bright intralayer moiré excitons at $\theta = 3.0°$, $2.0°$ and $1.5°$. The peaks are shown in FIG. S2.

First, we decompose the exciton amplitude to the contributions from each pair of conduction and valence bands, represented as $\sum_{\mathbf{k}} |A_{cv\mathbf{k}}|^2$ for a specific conduction band c and valence band v pairs (see Fig. S1). The exciton amplitudes projected onto the conduction and valence bands in the continuum model near the K valley are presented, and the projected amplitudes for the continuum model near the other valley exhibit a similar decay behavior. We find that the exciton amplitudes of the three bright intralayer moiré excitons that we focus on with $\theta = 2.5°$ [see Fig. 2(e) in the main text] are predominantly contributed by at most the first 20 conduction and valence bands (approximately ten pairs at each valley) [see Fig. S1(a)]. The projected amplitudes of the first two

bright moiré excitons (denoted in Fig. S2) on electron-hole pairs at other twist angles of $\theta = 1.5°$, 2.5° and 3.0° have also been tested, with results shown in Fig. S1(b-d) below. We can draw similar conclusions for these cases, confirming that the size of minibands used in our calculations is large enough.

Second, although it appears that a few electron-hole pairs can adequately describe the low-energy bright moiré excitons, we also test the exciton energy convergence with respect to the number of conduction and valence bands included in the construction of the BSE Hamiltonian matrix. We ensure that the peak energy of the ground moiré exciton state converges to approximately 1.0 meV, as shown in Fig. S2. Finally, for twist angles $\theta = 4.0°$, 3.0°, 2.5°, 2.0°, 1.5° and 1.0°, we use 15, 20, 25, 30, 40 and 60 conduction/valence minibands from the continuum model near each valley, respectively, throughout the article. This ensures that the low-energy bright moiré excitons are well described, achieving convergence of the ground state energy up to approximately 1.0 meV at each twist angle.

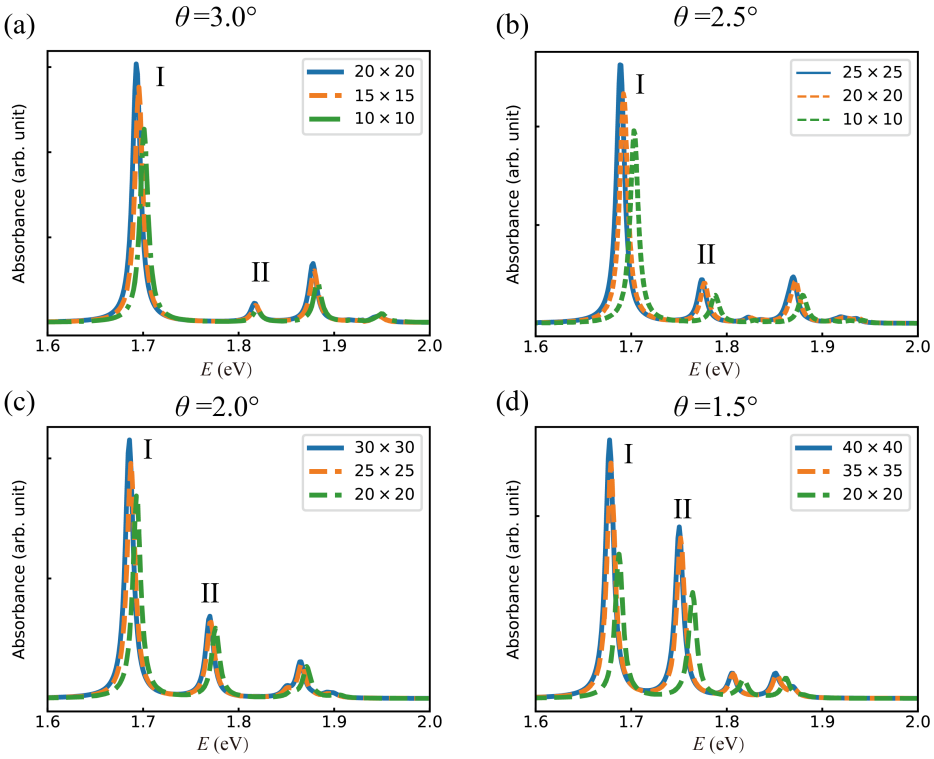

FIG. S2. (a-d) Convergence of the calculated absorption spectrum with the number of moiré conduction and valence bands in each valley at $\theta = 3.0°$, 2.5°, 2.0° and 1.5°. The legend indicates the number of conduction and valence bands used.

S5. TRIPLET-SINGLET SPLITTING

In this section, we focus on the triplet-singlet splitting of moiré excitons resulting from the Coulomb exchange interactions, as well as the spin-valley locking in TMD materials. As exotic properties in TMDs, the spin and valley degrees of freedom are coupled at the band edges, resulting in excitons that can be excited by circularly polarized light. In twisted TMD materials, the band folding introduces new moiré bands with opposite spins but similar energies on the band edges, leading to the emergence of new low-energy spin-triplet moiré excitons. We argue that the triplet-singlet splitting induced by the exchange interactions, which is important in unpolarized semiconductors

[14, 20], can occur in this context. More interestingly, the twist angle provides a new degree of freedom to tune these characteristics. To the best of our knowledge, such an effect has never been reported in moiré exciton systems, either theoretically or experimentally.

As shown in Fig. S3(a), we use the effective continuum models around the K and -K valleys in the BZ of untwisted TMD to calculate the moiré electronic structures for WSe_2 layer (see details in S1). Its moiré bands originating from the K and -K valleys are denoted by blue and red lines, respectively, and are folded into the moiré BZ. Due to the spin-valley locking in the original untwisted TMD materials, these bands [see blue and red lines in Fig. S3(b)] are spin-polarized. Considering the attractive Coulomb interaction, we predict that the spin-singlet bright moiré excitons are direct excitons and exhibit energy splitting from the spin-triplet moiré excitons. Furthermore, as shown in Fig. S3(a), if we only consider the energy positions of electrons and holes, the spin-triplet moiré excitons with $\mathbf{Q} = 0$ which have electrons originating from the continuum model near the -K valley and holes near the K valley [labeled as $|c, -\mathrm{K}; v, \mathrm{K}\rangle$ in Table S1 and the long red dashed line in Fig. S3(b)] seems to have higher energy than the singlet ones labeled as blue dashed line in Fig. S3 (b). However, based on our calculations which take into account the exchange Coulomb interactions, we find that the ordering of the moiré excitons and the splitting between spin-triplet and spin-singlet moiré excitons strongly depend on the twist angles.

At relatively large twist angles, for example, $\theta = 4.0^\circ$ shown in Fig. S3(e), the lowest energy bright spin-singlet moiré exciton has a similar energy to the spin-triplet moiré excitons and is nearly the ground state at zero momentum. Meanwhile, the lowest spin-triplet moiré exciton is indirect and has lower energy at finite momentum ($\mathbf{Q} \neq 0$) compared to its energy at zero momentum ($\mathbf{Q} = 0$). When the twist angle becomes smaller, the spin-triplet moiré excitons become the ground state even at zero momentum, exhibiting a flattened dispersion [see Fig. S3(c-e), the spin-singlet moiré excitons are labeled by blue lines and the spin-triplet ones by red lines], while the triplet-singlet splitting increases and appears to converge at small twist angles [see Fig. S3(f)]. We attribute this effect to the suppression of the kinetic energy of the electrons and holes. As the twist angle decreases, there is a reduced splitting in the band structure between the two spins [the energy difference between blue and red lines shown in Fig. S3(b)] becomes smaller. Consequently, the energy of the spin-triplet moiré excitons at zero exciton momentum decreases, and their dispersion becomes flat. Moreover, the spin-triplet excitons, where the electrons and holes originate from valleys with opposite spins, do not experience the Coulomb exchange interactions, which could contribute to an increase in the energy of the spin-singlet moiré excitons (see Table S1). As a result, the spin-triplet excitons will have lower energy than the spin-singlet ones at small twist angles, and the triplet-singlet (or dark-bright) splitting will increase as the twist angles decrease.

As highlighted in many previous studies [19, 21, 22], although dark excitons are not optically active and are difficult to observe directly in optical experiments, they can significantly influence the dynamics of excitons through exciton-phonon scattering or other non-radiative relaxation processes. Therefore, it is crucial to reveal the properties of dark excitons in moiré systems, including their binding energy and exciton band structures. According to our calculations, we deduce that bright moiré excitons at small twist angles will have a larger relaxation rate to the dark spin-triplet moiré excitons due to the increase in the triplet-singlet splitting. As the temperature rises, once the bright spin-singlet moiré excitons at small twist angles are optically pumped, they will have a greater equilibrium population, as they are higher in energy than the dark spin-triplet moiré excitons. However, at some larger twist angles, for example, when θ is larger than 4.0°, the population of bright spin-singlet moiré excitons may decrease with increasing temperature, as they become similar in energy to the dark spin-triplet moiré excitons and nearly the ground state. These effects will strongly influence the dynamic of moiré excitons, resulting in different optoelectronic properties.

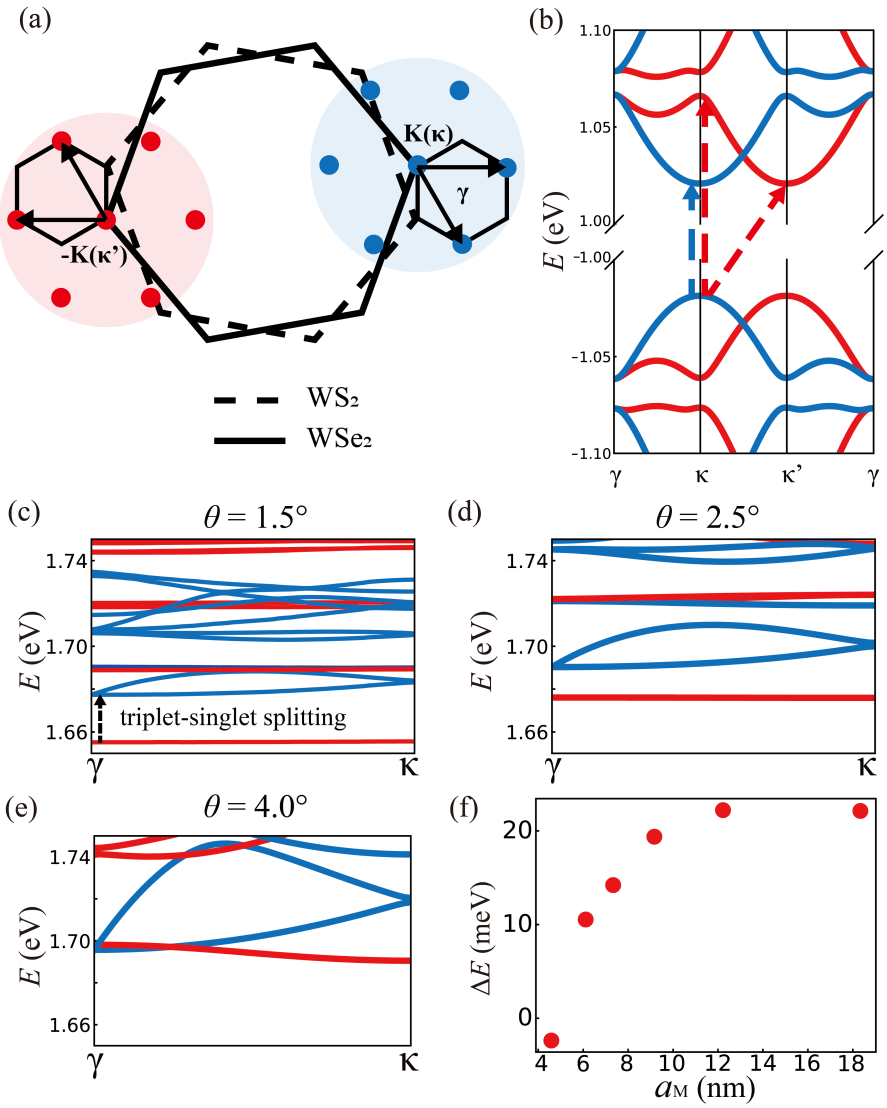

FIG. S3. (a) The BZ of twisted WSe_2/WS_2 heterostructures, and the moiré BZ of the moiré structures. K and -K points are momentum points in untwisted BZ. Blue and red dots are equivalent κ and κ' points in the moiré BZ. (b) The moiré band structure of WSe_2 layer in the twisted WSe_2/WS_2 heterostructures with $\theta = 4.0°$. The moiré band structures calculated from the effective continuum models around K and -K valleys of untwisted WSe_2 layer are denoted by blue and red lines, respectively. Due to the spin-valley locking in untwisted TMD materials, these blue and red lines stand for different spin-polarized states in the moiré BZ. The blue dashed line represents the formation of spin-singlet moiré exciton, while the red dashed lines represent the formation of spin-triplet moiré exciton. (c-e) The band structures of spin-singlet and spin-triplet moiré excitons at $\theta = 1.5°$, 2.5° and 4.0°, where the spin-singlet moiré excitons are labeled by blue lines and the spin-triplet ones by red lines. The physical meaning of the triplet-singlet splitting is denoted in (c). (f) The variation of the triplet-singlet splitting ΔE with different twist angles, or equivalently, with the moiré superlattice constant a_M.

S6. EFFECTS OF EXCHANGE INTERACTION ON INTERVALLEY COUPLING

In this section, we focus on the spin-singlet moiré excitons which correspond to the block $|c, \mathrm{K}; v, \mathrm{K}\rangle$ and $|c, -\mathrm{K}; v, -\mathrm{K}\rangle$, and ignore the spin-triplet ones. The advantage of the method proposed in this work over the previous continuum exciton model [4, 23] lies in its ability to resolve the effects of exchange interactions in the framework of BSE. We can modify the BSE by introducing a coefficient α, which varies from 0 to 1, to the exchange term.

$$H^{exc}_{vc\mathbf{k},v'c'\mathbf{k}'} = (E_{c\mathbf{k}} - E_{v\mathbf{k}})\delta_{c,c'}\delta_{v,v'}\delta_{\mathbf{k},\mathbf{k}'} + (f_{v\mathbf{k}} - f_{c\mathbf{k}})\left[\alpha\bar{V}_{vc\mathbf{k},v'c'\mathbf{k}'} - W_{vc\mathbf{k},v'c'\mathbf{k}'}\right] \tag{S10}$$

By solving these equations at different values of α, we can identify the evolution of each exciton band and observe the lifting of degeneracy of the lowest spin-singlet moiré excitons as a result of the intervalley exchange coupling introduced in S3 [See Fig. S4].

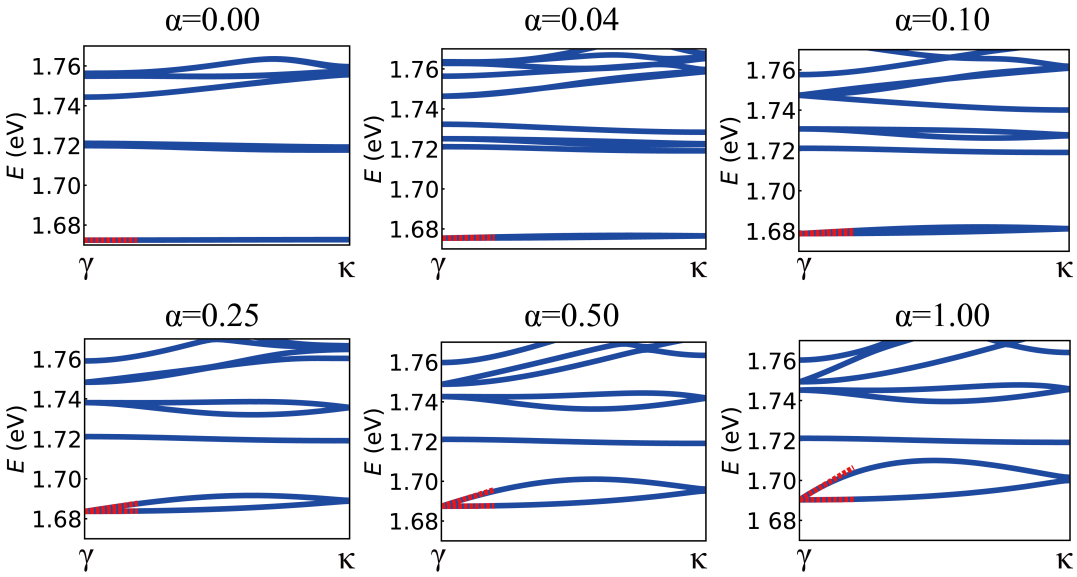

FIG. S4. The evolution of the bandstructure of WSe_2 intralayer moiré excitons in WSe_2/WS_2 with increasing exchange interactions. The value of α represents the strength of the exchange interaction, varying from 0 to 1.

S7. THE ESTIMATION OF THE RATE OF VALLEY DEPOLARIZATION

As shown in previous research on exciton of monolayer TMDs [12, 24, 25], the splitting of the lowest spin-singlet 1s-excitons with the center-of-mass momentum $\mathbf{Q}$ near γ ($\mathbf{Q}$=0) from two opposite valleys can be described by a two-band effective Hamiltonian within the basis of excitons from two valleys

$$\hat{H}_{\mathbf{Q}} = \Omega_0\hat{\sigma}_0 + A|\mathbf{Q}|[\hat{\sigma}_0 + \cos(2\theta)\hat{\sigma}_x + \sin(2\theta)\hat{\sigma}_y] + \left[\left(\frac{\hbar^2}{2M} + \alpha + \beta\right)\hat{\sigma}_0 + \beta'(\hat{\sigma}_x + \hat{\sigma}_y)\right]Q^2 \quad \text{(S11)}$$

where $\sigma_0, \sigma_{x,y}$ are the identity and Pauli matrix, respectively, M is the effective mass of the moiré excitons, $\hbar$ is the reduced Planck's constant, Ω_0 is the binding energy of the lowest 1s state for the spin-singlet moiré exciton with $Q = 0$, A is the constant representing the dominant order of the exchange coupling, the α, β, and β' are the constants of Q^2 order originating from the both direct and exchange Coulomb interactions [12]. Via solving this Hamiltonian, we can obtain a parabolic band structure for the lower band and a nonanalytic linear dispersion for the upper band.

$$\begin{aligned}\Omega_l(\mathbf{Q}) =& \Omega_0 + \left(\frac{\hbar^2}{2M} + \alpha + \beta - |\beta'|\right)Q^2 \\ \Omega_u(\mathbf{Q}) =& \Omega_0 + 2A|\mathbf{Q}| + \left(\frac{\hbar^2}{2M} + \alpha + \beta + |\beta'|\right)Q^2\end{aligned} \quad \text{(S12)}$$

The stronger the coupling between moiré excitons from the two valleys, the faster the exciton depolarizes to the opposite valley. For simplicity, we can estimate the rate of valley depolarization of

exciton states with momentum $\mathbf{Q}$ as $\Gamma_{v\mathbf{Q}} = \frac{2A|\mathbf{Q}|}{\hbar}$ [24], and the average valley depolarization rate in the light cone can be estimated as

$$\Gamma_v = \frac{2\pi}{\tau_v} = \frac{\int_{l.c.} d\mathbf{Q}\Gamma_{v\mathbf{Q}}}{\int_{l.c.} d\mathbf{Q}} = \frac{4AQ_c}{3\hbar} \tag{S13}$$

where $l.c.$ means the integral is performed in the light cone $|\mathbf{Q}| < Q_c$. The average valley depolarization rate is proportional to the coupling strength A. Finally, the degree of circular polarization P can be expressed as [26]

$$P = \frac{P_0}{1 + 2\tau_{re}/\tau_v} \tag{S14}$$

where the τ_{re} represents the recombination rate of the excitons, and the estimated results are displayed in Fig. 4(e) in the main text.

S8. TWSIT ANGLE-DEPENDENT BOHR RADUIS

In this section, we focus on the spin-singlet moiré excitons. In addition to the behavior of the twist angle-dependence of the binding energy and the exchange coupling strength discussed in the main text, our method proposed in this work also allows us to investigate the variation of the real-space wavefunctions of the moiré excitons with the change of the moiré period. Herein, we focus on the peak I of the moiré excitons with an isotropic hydrogen-like envelope. The hole position $\mathbf{r}_h$ is fixed at the Se/W and the wavefunction is assumed to be approximated by $|\Psi(\mathbf{r_e}, \mathbf{r_h})|^2 \sim \exp(-|\mathbf{r}_e - \mathbf{r}_h|/a_B)$. As shown in Fig. S5(a), we calculate the real space wavefunctions of peak I excitons at various twist angles ranging from $\theta = 1.0°$ to $4.0°$. The Bohr radius a_B can be further fitted and plotted in Fig. S5(b). We can observe that the Bohr radius increases with the enlarging of the moiré period as the twist angle is decreased. We argue that the Bohr radii of WSe_2 intralayer excitons in twisted WSe_2/WS_2 heterostructures can be compared with the future experimental observations directly, such as the optical spectroscopy and the time- and angle-resolved photoemission spectroscopy (trARPES) [27, 28].

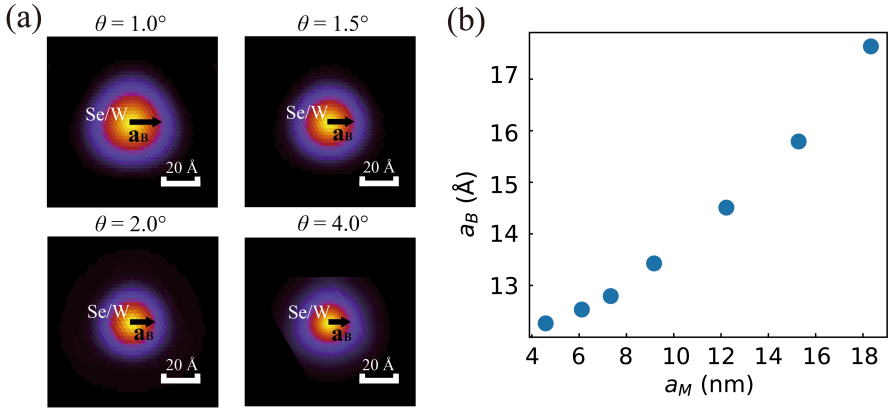

FIG. S5. (a) The real space wavefunctions $|\Psi(\mathbf{r_e}, \mathbf{r_h})|^2$ of peak I moiré excitons with the hole fixed at the Se/W region (similiar to Fig. 2(f) in the main text) at $\theta = 1.0°, 1.5°, 2.5°$ and $4.0°$. (b) The dependence of the Bohr radius a_B of the peak I moiré excitons on the moiré period a_M.

[1] D. Xiao, G.-B. Liu, W. Feng, X. Xu, and W. Yao, Coupled spin and valley physics in monolayers of MoS_2 and other group-VI dichalcogenides, Phys. Rev. Lett. **108**, 196802 (2012).

[2] J. Li, D. Zhai, C. Xiao, and W. Yao, Dynamical chiral Nernst effect in twisted van der Waals few layers, Quantum Front. **3**, 11 (2024).

[3] M. H. Naik, E. C. Regan, Z. Zhang, Y.-H. Chan, Z. Li, D. Wang, Y. Yoon, C. S. Ong, W. Zhao, S. Zhao, *et al.*, Intralayer charge-transfer moiré excitons in van der Waals superlattices, Nature **609**, 52 (2022).

[4] F. Wu, T. Lovorn, and A. H. MacDonald, Topological exciton bands in moiré heterojunctions, Phys. Rev. Lett. **118**, 147401 (2017).

[5] H. Yu, G.-B. Liu, J. Tang, X. Xu, and W. Yao, Moiré excitons: From programmable quantum emitter arrays to spin-orbit–coupled artificial lattices, Sci. Adv. **3**, e1701696 (2017).

[6] G. Kresse and J. Hafner, *Ab initio* molecular dynamics for liquid metals, Phys. Rev. B **47**, 558 (1993).

[7] G. Kresse and J. Furthmüller, Efficiency of ab-initio total energy calculations for metals and semiconductors using a plane-wave basis set, Comput. Mater. Sci. **6**, 15 (1996).

[8] G. Kresse and J. Furthmüller, Efficient iterative schemes for ab initio total-energy calculations using a plane-wave basis set, Phys. Rev. B **54**, 11169 (1996).

[9] J. P. Perdew, K. Burke, and M. Ernzerhof, Generalized gradient approximation made simple, Phys. Rev. Lett. **77**, 3865 (1996).

[10] F. Wu, T. Lovorn, E. Tutuc, I. Martin, and A. H. MacDonald, Topological insulators in twisted transition metal dichalcogenide homobilayers, Phys. Rev. Lett. **122**, 086402 (2019).

[11] G. Onida, L. Reining, and A. Rubio, Electronic excitations: density-functional versus many-body Green's-function approaches, Rev. Mod. Phys. **74**, 601 (2002).

[12] D. Y. Qiu, T. Cao, and S. G. Louie, Nonanalyticity, valley quantum phases, and lightlike exciton dispersion in monolayer transition metal dichalcogenides: Theory and first-principles calculations, Phys. Rev. Lett. **115**, 176801 (2015).

[13] M. Rohlfing and S. G. Louie, Excitonic effects and the optical absorption spectrum of hydrogenated Si clusters, Phys. Rev. Lett. **80**, 3320 (1998).

[14] M. Rohlfing and S. G. Louie, Electron-hole excitations and optical spectra from first principles, Phys. Rev. B **62**, 4927 (2000).

[15] L. V. Keldysh, Coulomb interaction in thin semiconductor and semimetal films, JETP Lett. **29**, 658 (1979), [Pis'ma Zh. Eksp. Teor. Fiz. 29, 716 (1979)].

[16] A. Chernikov, T. C. Berkelbach, H. M. Hill, A. Rigosi, Y. Li, B. Aslan, D. R. Reichman, M. S. Hybertsen, and T. F. Heinz, Exciton binding energy and nonhydrogenic rydberg series in monolayer WS_2, Phys. Rev. Lett. **113**, 076802 (2014).

[17] E. Mostaani, M. Szyniszewski, C. H. Price, R. Maezono, M. Danovich, R. J. Hunt, N. D. Drummond, and V. I. Fal'ko, Diffusion quantum Monte Carlo study of excitonic complexes in two-dimensional transition-metal dichalcogenides, Phys. Rev. B **96**, 075431 (2017).

[18] M. Szyniszewski, E. Mostaani, N. D. Drummond, and V. I. Fal'ko, Binding energies of trions and biexcitons in two-dimensional semiconductors from diffusion quantum Monte Carlo calculations, Phys. Rev. B **95**, 081301 (2017).

[19] G. Wang, A. Chernikov, M. M. Glazov, T. F. Heinz, X. Marie, T. Amand, and B. Urbaszek, Colloquium: Excitons in atomically thin transition metal dichalcogenides, Rev. Mod. Phys. **90**, 021001 (2018).

[20] D. Y. Qiu, F. H. da Jornada, and S. G. Louie, Solving the bethe-salpeter equation on a subspace: Approximations and consequences for low-dimensional materials, Phys. Rev. B **103**, 045117 (2021).

[21] M. Selig, G. Berghäuser, M. Richter, R. Bratschitsch, A. Knorr, and E. Malic, Dark and bright exciton formation, thermalization, and photoluminescence in monolayer transition metal dichalcogenides, 2D Mater. **5**, 035017 (2018).

[22] Y. Jiang, S. Chen, W. Zheng, B. Zheng, and A. Pan, Interlayer exciton formation, relaxation, and transport in TMD van der Waals heterostructures, Light Sci. Appl. **10**, 72 (2021).

[23] F. Wu, T. Lovorn, and A. MacDonald, Theory of optical absorption by interlayer excitons in transition metal dichalcogenide heterobilayers, Phys. Rev. B **97**, 035306 (2018).

[24] H. Yu, G.-B. Liu, P. Gong, X. Xu, and W. Yao, Dirac cones and Dirac saddle points of bright excitons in monolayer transition metal dichalcogenides, Nat. Commun. **5**, 3876 (2014).

[25] C. Li and W. Yao, Chiral excitonic systems in twisted bilayers from Förster coupling and unconventional excitonic Hall effects, Phys. Rev. B **110**, L121407 (2024).

[26] K. F. Mak, K. He, J. Shan, and T. F. Heinz, Control of valley polarization in monolayer MoS_2 by optical helicity, Nat. Nanotechnol. **7**, 494 (2012).

[27] D. Schmitt, J. P. Bange, W. Bennecke, A. AlMutairi, G. Meneghini, K. Watanabe, T. Taniguchi, D. Steil, D. R. Luke, R. T. Weitz, *et al.*, Formation of moiré interlayer excitons in space and time, Nature **608**, 499 (2022).

[28] M. K. Man, J. Madéo, C. Sahoo, K. Xie, M. Campbell, V. Pareek, A. Karmakar, E. L. Wong, A. Al-Mahboob, N. S. Chan, *et al.*, Experimental measurement of the intrinsic excitonic wave function, Sci. Adv. **7**, eabg0192 (2021).